

Automatic Vessel Segmentation Using Active Contours in Cine Phase Contrast Flow Measurements

Sebastian Kozerke, MSc,¹ René Botnar, PhD,¹ Sten Oyre, MD,²
Markus B. Scheidegger, PhD,¹ Erik M. Pedersen, MD, PhD,² and Peter Boesiger, PhD^{1*}

The segmentation of images obtained by cine magnetic resonance (MR) phase contrast velocity mapping using manual or semi-automated methods is a time consuming and observer-dependent process that still hampers the use of flow quantification in a clinical setting. A fully automatic segmentation method based on active contour model algorithms for defining vessel boundaries has been developed. For segmentation, the phase image, in addition to the magnitude image, is used to address image distortions frequently seen in the magnitude image of disturbed flow fields. A modified definition for the active contour model is introduced to reduce the influence of missing or spurious edge information of the vessel wall. The method was evaluated on flow phantom data and on in vivo images acquired in the ascending aorta of humans. Phantom experiments resulted in an error of 0.8% in assessing the luminal area of a flow phantom equipped with an artificial heart valve. Blinded evaluation of the volume flow rates from automatic vs. manual segmentation of gradient echo (FFE) phase contrast images obtained in vivo resulted in a mean difference of $-0.9 \pm 3\%$. The mean difference from automatic vs. manual segmentation of images acquired with a hybrid phase contrast sequence (TFEPI) within a single breath-hold was $-0.9 \pm 6\%$. J. Magn. Reson. Imaging 1999; 10:41-51. © 1999 Wiley-Liss, Inc.

Index terms: flow quantification; image segmentation; aortic flow

MR CINE PHASE contrast flow measurements have been proved to be a reliable method for the assessment of flow-related parameters in larger vessels (1-3). However, the evaluation of the acquired images is a time-

consuming process that still hampers the use of flow quantification in a clinical setting. The calculation of flow parameters requires the delineation of the vessel cross section in a time series of velocity-encoded images. Defining the vessel boundaries manually, which is considered as the gold standard, lasts unacceptably long in clinical practice and is subject to observer-dependent variability (4).

Several approaches for vessel segmentation of MR phase contrast images have been reported. Magnitude masking is often used (4). However, the threshold calculated for image masking depends on pixel statistics within certain regions defined by the user. Also, the loss of signal due to disturbed inflow or intra-voxel dispersion might affect the mask determination and necessitates additional user interaction.

Since vessel boundaries in MR images are assumed to be closed and smooth, the set of possible shapes can be restricted to continuous contours. Such controllable active contours for image segmentation were introduced by Kass et al (5). Recently, active contour-based segmentation has been used to extract vessel boundaries in MR phase contrast image sequences of the ascending aorta (6) and the carotid arteries (7). Both approaches use the final contour from a previously processed temporal neighboring frame as an initial seed for the subsequent frame to be processed. However, in case of considerable change in position and shape of the vessel cross section between subsequent frames, as seen for the ascending aorta, the propagation may introduce errors if the seed contour is too far away from the boundary to be segmented. Disturbed flow conditions and partial volume effects at the vessel wall often degrade the vessel boundary representation in MR images. To address these problems, an algorithm using multiresolution analysis based on the wavelet transform was presented in ref. 8.

However, all algorithms proposed so far were only applied to magnitude images. Since signal loss degrading the vessel wall representation in MR images is often seen in measurements downstream of heart valves, the methods may fail on images mapping disturbed flow fields. Signal loss can be caused by the presence of turbulence, which is considered an indication of some

¹Institute of Biomedical Engineering and Medical Informatics, University of Zurich and Swiss Federal Institute of Technology, 8092 Zurich, Switzerland.

²Department of Cardiothoracic and Vascular Surgery and Institute of Experimental Clinical Research, MR Center, Aarhus University Hospital, 8200 Aarhus, Denmark.

Grant sponsor: EUREKA; Grant number: EU 1353; Grant sponsor: Swiss Commission for Technology and Innovation; Grant number: 3030; Grant sponsor: Danish Heart Foundation; Grant number: 97-2-1-5-22549; Grant sponsor: Philips Medical Systems (Best, The Netherlands).

Presented in part at the 4th and 5th Scientific Meetings of ISMRM, 1996, 1997.

*Address reprint requests to: P.B., Institute of Biomedical Engineering and Medical Informatics, University and ETH Zurich, Gloriastrasse 35, 8092 Zurich, Switzerland. E-mail: boesiger@biomed.ee.ethz.ch

Received November 4, 1998; Accepted March 18, 1999.

© 1999 Wiley-Liss, Inc.

type of abnormality (9), but has also been observed in MR images obtained in healthy elderly subjects (10). In general, blood flow disturbance often occurs immediately downstream of a normal functioning native aortic valve with normal cardiac output (11).

We hypothesized that fully automatic vessel segmentation of MR phase contrast images for calculation of blood flow throughout the cardiac cycle with minimal initial user interaction can be accomplished by using active contour-based segmentation in combination with dedicated improvements. To achieve high accuracy and reproducibility of the segmentation the following features were introduced:

1. The phase instead of the magnitude image is used for segmentation of time frames that are subject to flow-related signal loss.
2. A new definition of the active contour model propagates contour similarity of consecutive time frames to make the model less sensitive to missing or spurious edge features.
3. To take into account the non-abrupt transition from vessel lumen to wall due to inflow and partial volume effects, a correction scheme for edge detection is introduced to circumvent underestimation of cross-sectional vessel area.

The proposed algorithm was applied to images obtained in a flow phantom downstream of an artificial heart valve in a steady flow setup and to in vivo images of the ascending aorta of healthy volunteers acquired with a conventional phase contrast sequence and with a fast hybrid technique allowing for single breath-hold acquisition.

MATERIALS AND METHODS

Image Characteristics

MR phase contrast imaging uses the phase shift of the MR signal of spins moving along a magnetic field gradient for velocity encoding. Velocity information is given in the images as a gray scale representation of the acquired phase shifts. Anatomic information is contained in the magnitude of the acquired signal. Gradient-echo imaging of blood flow is subject to the following flow-related characteristics:

1. The parabolic velocity distribution within the small boundary layer near the vessel wall causes signal decrease within this layer going toward the wall. Voxels at the vessel wall might contain signal from both moving blood and the stationary vessel

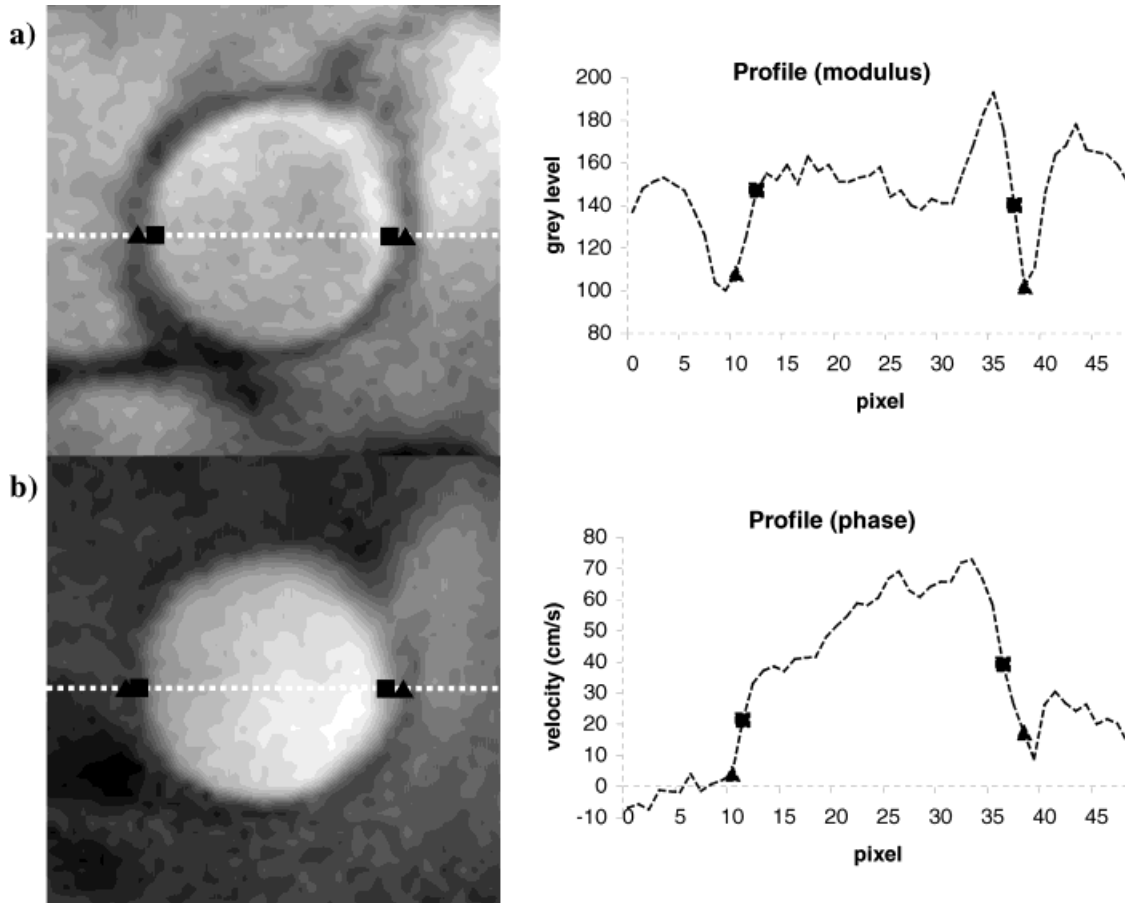


Figure 1. Profile of the magnitude (a) and the phase (b) image obtained perpendicular to the ascending aorta during flow acceleration. Intensity profiles across the same diameter (white dotted line) are given for the magnitude and phase image. Points of local maximum image gradients are indicated (■). Contour points (▲) marked manually are shifted outward with respect to the automatically detected points.

wall. Thus, edge points detected at local maximum image gradients as a result of standard edge detection filters (12) are located slightly inside the vessel lumen and not exactly at the vessel wall (Fig. 1).

2. Dispersion of signal phase due to non-uniform velocity distribution within a single voxel leads to signal loss. This can be caused by strong spatial variation of velocity across the imaging slice and by random spatial and temporal variation of velocity in regions of turbulence.

Figure 2 shows the magnitude and the phase image obtained at peak systole downstream of the aortic valve in a healthy young volunteer. Extracted edge points are overlaid to demonstrate the influence of image distortion in a pair of magnitude and phase images. Whereas no meaningful edge information could be extracted from the magnitude image, considerable parts of the vessel boundary were accurately identified in the phase image.

To investigate further the different degradation of the magnitude and the phase image in a disturbed flow field, computer simulations were carried out. A turbulent steady flow field with a maximum velocity of 110 cm/sec was simulated with fluctuation velocity $u'(t)$. The root mean square of $u'(t)$ was 13.2 cm/sec, giving a relative turbulence intensity of 15%; the vessel diameter was 20 mm. The MR readout experiment was performed to obtain the complex signal in k -space. The following parameters were used: spatial resolution $1 \times 1 \text{ mm}^2$, echo time 5.7 msec, and velocity encoding 120 cm/sec. Figure 3 indicates the stability of the phase in contrast to the magnitude of the MR signal obtained in the simulated flow field. Since the signal phase remains more stable than magnitude, the segmentation would benefit from using the phase instead of magnitude in frames that are subject to intra-voxel dispersion.

Theory of Active Contours

The active contour paradigm, as originally proposed in ref. 5, describes a deformable contour balancing two different energy fields:

1. Internal energy determines the stretching and bending behavior of the contour. It keeps a smooth contour shape under forces derived from the external energy field by penalizing sharp bends and large stretching.
2. External energy is characterized by image forces attracting the contour to the desired boundaries. Image forces are derived from the *feature image* (eg, the edge map of the original image data).

In the following discussion a brief overview of the active contour paradigm is given. The closed contour in the image plane is defined by $\gamma(s, t)$, where s is a spatial parameter and t denotes time defined over given intervals Ω and T , respectively. When adapting the contour to the feature image, the total contour energy $E(\gamma)$, being the sum of the internal contour energy $E_{\text{int}}(\gamma)$ and the external energy $E_{\text{ext}}(\gamma)$, must approach a minimum. To control the stretching and bending behavior of the contour, the internal energy is defined according to ref 5:

$$E_{\text{int}}(\gamma) = \frac{1}{2} \int_{\Omega} (w_1 \|\gamma_s(s)\|^2 + w_2 \|\gamma_{ss}(s)\|^2) ds. \quad (1)$$

The parameters w_1 and w_2 are used to weight the magnitude of the first $[\gamma_s(s)]$ and second $[\gamma_{ss}(s)]$ spatial derivative of the contour and thereby control the elasticity and rigidity.

The external energy term is associated with the feature image $\text{img}(\gamma)$:

$$E_{\text{ext}}(\gamma) = \int_{\Omega} \text{img}(\gamma) ds. \quad (2)$$

Using a discrete representation $U = (X, Y)^T = (x_0 \dots x_{N-1}, y_0 \dots y_{N-1})^T$ of the contour, with N uniformly

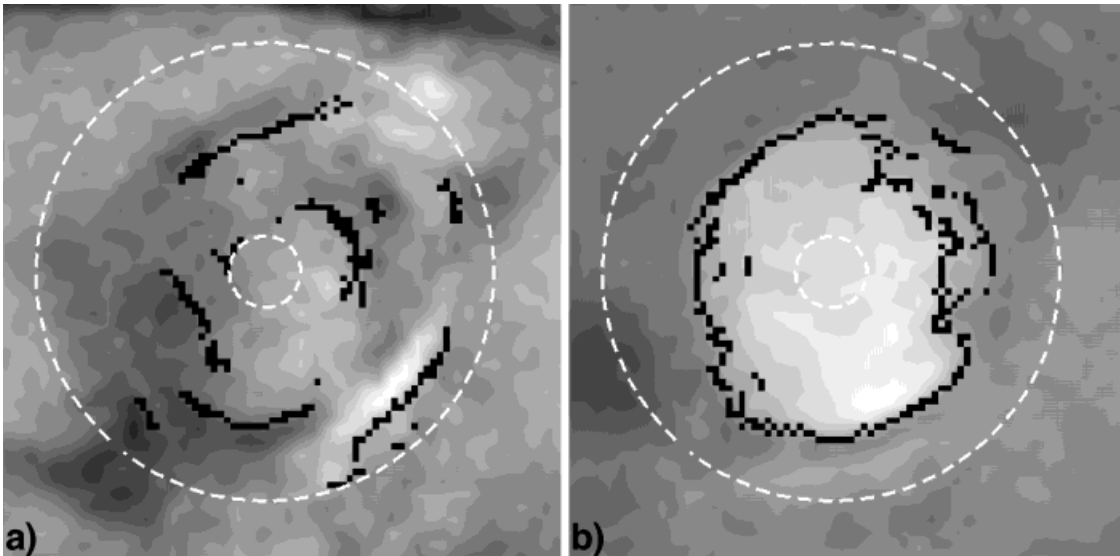


Figure 2. Magnitude (a) and phase (b) image obtained at peak systole. Local maximum image gradients, which were extracted within the bounds given by the dashed circles, are overlaid. Image distortion seen in the magnitude leads to insufficient edge detection, whereas most parts of the vessel boundary are extracted using the phase image.

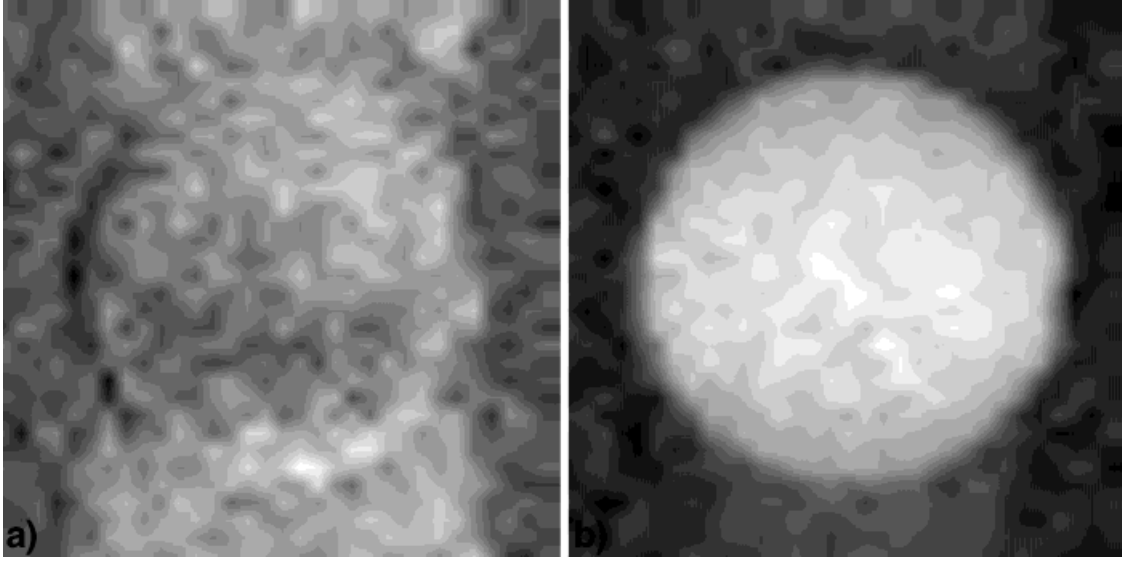


Figure 3. Numerical simulation of intra-voxel dispersion effects due to turbulent flow. The maximum velocity of parabolic flow field was 110 cm/sec, and the root mean square of the fluctuation velocity was 13.2 cm/sec. Whereas the vessel wall representation in the magnitude image is severely distorted (a), the vessel boundary in the phase image is still recognizable (b).

spaced nodes, the derivatives of the contour can be approximated by a finite difference scheme. Introducing the stiffness matrix K , the internal energy can be rewritten in matrix notation:

$$E_{\text{int}}(U) = \frac{1}{2} U^T K U. \quad (3)$$

The total contour energy $E(U)$ must be minimized to find the optimal shape and position on the feature image. This can be achieved by solving the associated Euler-Lagrange differential equation (see Appendix for a detailed description):

$$M\ddot{U} + C\dot{U} + KU = F(U)$$

with

$$F(U) = k_0 \vec{n}(X, Y) - k_1 \frac{\nabla \text{img}(X, Y)}{\|\nabla \text{img}(X, Y)\|}. \quad (4)$$

M introduces the mass density of the contour and C the damping constant of the system. $F(U)$ includes a force pushing the contour in the outer normal direction, which is added to the normalized force generated by the feature image, as suggested in ref. 13. The force directed in the outer normal direction is scaled with k_0 and must be smaller than the force arising from the image features, which is scaled with k_1 to prevent stepping over meaningful edges. $\vec{n}(X, Y)$ denotes the unity vectors perpendicular to the contour.

Automatic Vessel Segmentation

The following concepts were chosen to obtain automatic vessel segmentation.

1. To ensure robust segmentation of the first image frame (*start frame processing*), the initial active

contour runs on the image frame corresponding to the early systolic acceleration of blood flow. In this frame blood flow is expected to be unidirectional.

2. Processing the remaining time frames sequentially (*sequential frame processing*), a previously segmented, temporally neighboring contour is used for the actual frame as a model for segmentation to approximate the contour in case of missing or distorted edge features.
3. Because the active contour model is inherently restricted to local features, the initial seed contour for each frame has to be in the vicinity of the desired vessel boundary. However, larger arteries such as the ascending aorta change their position during the cardiac cycle. Therefore, the position of the seed contour has to be adjusted for each image frame of the cardiac cycle.
4. Anatomy in the vicinity of the vessel of interest may contribute strong edge features near the vessel wall. Such edge points could trap the active contour. Therefore, the contour is pulled from inside the vessel lumen towards the vessel wall.

Start Frame Processing

The approximate center of the vessel of interest is manually selected in an arbitrary image frame. Then the phase image at the phase corresponding to the early systolic acceleration of blood flow is automatically searched for to serve as the first frame to be processed. This is accomplished by a) convoluting each phase frame with a gaussian mask for noise reduction; b) detecting all pixels of each phase image that exceed half of the maximum phase as found within a circular mask around the selected vessel center; c) removing isolated pixels and filling holes using connectivity criteria; and d) selecting the first phase image in time with an area of half of the maximum found overall. Furthermore, from

this initial starting frame, the diameter and position of the circular initial seed contour for the subsequent active contour segmentation are derived. In addition, two parameters describing the contour displacement and the change in shape, which is allowed for temporally consecutive time frames, are set. A given contour is then reduced and dilated in size with a radial offset equal to the parameters to obtain inner and outer boundaries. Accordingly, the contour displacement and change in shape is restricted by considering only the area between the inner and the outer boundaries.

Feature Image Calculation

To address the variable transition between vessel lumen and wall, a modified edge detection is applied. Using anisotropic diffusion filtering (14), the noise of the actual image frame is reduced. After noise filtering, local maximum image gradients are searched in a radial manner normal to the contour within the boundaries restricting contour displacement. Only local maximum image gradients at transitions from bright to dark in the magnitude image and high absolute velocity to low absolute velocity in the phase image are detected. Detected edge points are reduced to a single pixel width by suppressing non-maximums. Furthermore, for each edge point, calculated on the phase image (*pha*), a correction is applied by assuming a linear transition from the vessel lumen to the wall within the small boundary layer near the vessel wall:

$$\Delta r(\varphi) = \frac{pha_0 - pha(r, \varphi)}{\frac{\partial}{\partial r} pha(r, \varphi)}. \quad (5)$$

The corrected edge point is shifted by $\Delta r(\varphi)$ with respect to the detected edge point along the direction of the radial gradient search \vec{e}_φ to the cut-point of the linear approximation with the zero phase (pha_0) (Fig. 4a). For the magnitude image, the corrected edge point is found by incrementing $\Delta r(\varphi)$ until a concave image transition is reached (Fig. 4b).

Start Frame Segmentation (Active Contour I)

Discretizing the temporal derivatives of vector U in Eq. [4], the position updates of the contour points for a

specified time step Δt are calculated. If the mass density M is assumed to be zero and $F(U_{t+\Delta t}) \equiv F(U_t)$, the solution for vector U is found by:

$$U_{t+\Delta t} = (C + K\Delta t)^{-1} (CU_t + F(U_t) \Delta t). \quad (6)$$

The equation is solved iteratively until the energy fluctuation of subsequent loops is below a certain threshold (15). To avoid bunching of contour points, resampling is used after each iteration to keep a uniform spacing of the contour nodes. An optional refinement step lets the user interact by identifying points to which the contour should stick. Marked points are introduced into the feature image as minima and attract the contour in a subsequent re-run of the active contour. The steps applied for *start frame processing* are illustrated in Fig. 5.

Sequential Frame Processing

Depending on the average velocity as estimated within the layer defined by the inner boundary restricting contour displacement, the decision of whether to use the phase image in addition to the magnitude image for *feature image calculation* is made. If the estimated velocity exceeds 30% of the maximum velocity as estimated during the *start frame processing* step, the feature map of the phase image is additionally generated.

Determination of Vessel In-Plane Displacement

By calculating the correlation of a given contour kernel $K(i, j)$, $0 \leq i \leq I$, $0 \leq j \leq J$ with the feature map of the current image frame $M(m, n)$, $0 \leq m \leq M$, $0 \leq n \leq N$, the vessel displacement between the current and previously processed frame is obtained:

$$C(m, n) = -M_{mn}^2 \star K + 2M_{mn} \star K. \quad (7)$$

Basically, the nearest (with respect to the gravity center of the model contour) local maximum of Eq. [7] is determined and used for calculating the displacement. The contour kernel is a bitmap representation of the contour segmented on the previously processed temporally neighboring frame. I, J denote the width and height of the rectangular map capturing the kernel. The allowed displacement is restricted according to the param-

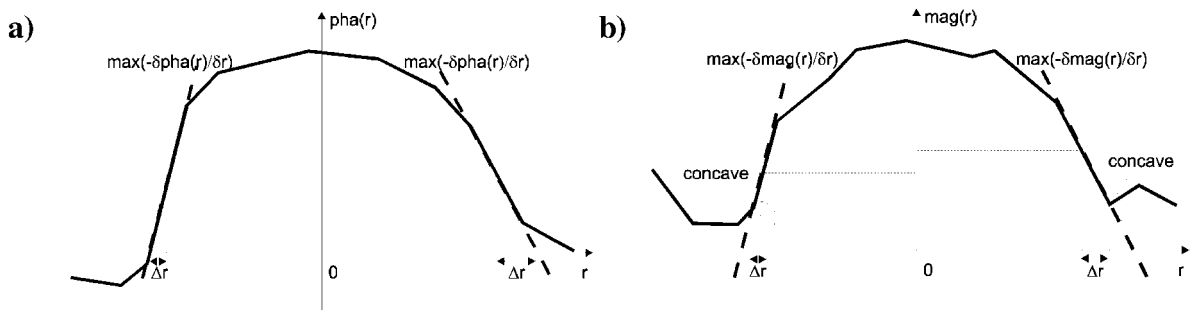


Figure 4. Correction of edge points detected at positions of local maximum image gradients. Edge points of the phase image (*pha*) are shifted by Δr to the cross-point of the approximated velocity distribution near the wall with the line of zero velocity (a). The magnitude image (*mag*) edge points are shifted, starting from the point of the local maximum gradient, in the outer radial direction to the first occurrence of a concave image transition (b).

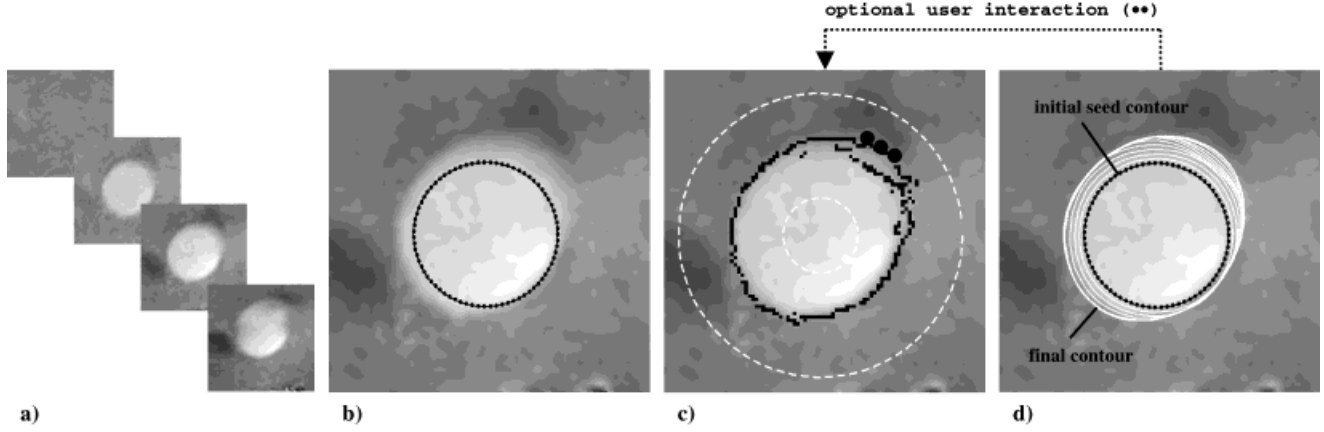


Figure 5. Start frame segmentation. The phase frame corresponding to the early systolic acceleration of blood flow is automatically chosen as the initial frame for segmentation (a). From the initial frame the position and size of the circular seed contour is derived. The seed contour is placed on the initial frame (b). Radial edge detection is performed within the bounds determined by the parameter restricting the frame-to-frame contour displacement (dashed contours) (c). The initial seed is pulled toward the vessel wall using the active contour (d). Suboptimal segmentation results may be corrected by introducing local minima (indicated by the black dots) into the edge map (c) and restarting the active contour (d).

eter set during *start frame processing* and determines the bounds M , N .

Modulus Versus Phase Selection

By default the feature image generated from the magnitude image is used for segmentation. However, if the phase image was additionally processed and the degree of correlation calculated for the phase image is above the correlation found for the magnitude image, the feature image generated from the phase image is used for segmentation instead.

Sequential Frame Segmentation (Active Contour II)

A new constraint for the internal energy term $E_{\text{int}}(U)$ is introduced to take into account the model of the contour to be searched for. In case of missing edge features in the current frame, the contour is approximated by the model shape. The influence of spurious edges is reduced by penalizing a contour shape and position differing too much from the model shape:

$$E_{\text{int}}(U) = \frac{1}{2} (U_{\text{model}} - U)^T (K + \lambda I) (U_{\text{model}} - U). \quad (8)$$

As model U_{model} , the contour of the previously processed temporally neighboring image frame, which is corrected for the displacement component, is used. The parameter λ controls the force between the actual and the model contour and thereby determines the similarity of the actual and the model contour. Using the definition for $E_{\text{int}}(U)$, vector U is now calculated as follows:

$$U_{t+\Delta t} = (C + K\Delta t + \lambda I\Delta t)^{-1} \cdot [CU_t + (K\Delta t + \lambda I\Delta t) U_{\text{model}} + F(U) \Delta t]. \quad (9)$$

The previously described steps are repeated in a loop to process successively all remaining heart phases of the cardiac cycle (Fig. 6). An overview of the processing steps for segmentation is given in Fig. 7.

Before calculating blood flow, the MR phase data are corrected for phase shifts caused by eddy currents. Phase correction is accomplished by subtracting a plane obtained by a least-square fit through the phase values of stationary tissue. After final interpolation of the contour nodes by cubic polynomials, volume blood flow is calculated by integration of all pixel velocities within the contour.

Parameter Determination

The scaling for the internal features of the model w_1 and w_2 is kept constant for all contour nodes and iterations. They are adjusted to values on the order of h^2 and h^4 , as proposed in ref. 16, h denoting the inter-nodal distance of the contour. Forces derived from image features are scaled with $k_1 = 1.0$. The force directed to the outer normal direction of the contour is weighted by $k_0 = 0.9$ k_1 and is only incorporated into the *start frame segmentation* step. The remaining parameters are set as follows: $\gamma = 2.0$, $\lambda \propto 1/\text{shape_restriction}$, and the time step Δt is 1.0. The *shape_restriction* reflects the allowed maximum change of the vessel shape for two temporally neighboring image frames.

Manual Contour Extraction

By visual inspection of the cross-sectional magnitude images and the corresponding phase images, points were placed manually on the assumed vessel wall. Blood flow was calculated by integration of all pixel velocities within the cubic polynomial fitted through the marked points.

Phantom Measurements

A Plexiglas pipe equipped with a bileaflet artificial heart valve was used in a steady flow setup ($Q = 15$ l/min). Fluid viscosity and relaxation constants T_1 , T_2 were matched to the values of blood (3.53 mPas, 941.1/232.2

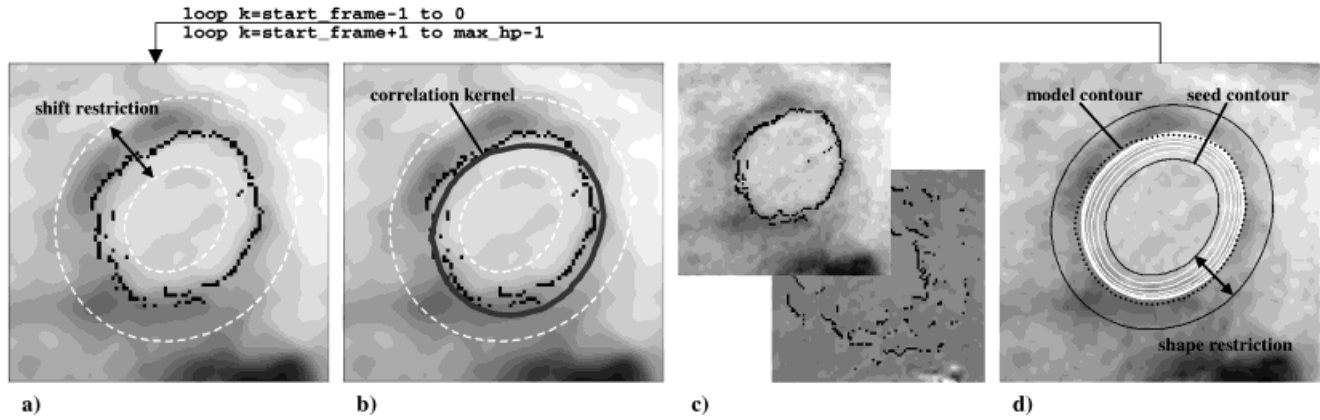


Figure 6. Sequential frame segmentation. For the current time frame k , edge detection is performed on the modulus image and additionally, if the estimated flow rate is above a threshold, on the phase image within the bounds restricting frame-to-frame contour displacement (dashed contours) (a). The actual displacement and the degree of correlation with respect to the previously segmented temporally neighboring contour is determined (b). In case edge detection was additionally performed on the phase image, the decision whether to use the magnitude or phase image for segmentation is made based on the degree of correlation (c). Finally, the current frame is segmented with an active contour scheme incorporating the contour of the temporally neighboring time frame as a model shape (dotted contour) (d).

msec). The internal diameter of the pipe was 40 mm. Velocity was mapped at three axial distances downstream to the valve ($x = 8, 160, 212$ mm). For these locations the flow conditions were known from measurements performed using laser Doppler anemometry.

At the first location ($x = 8$ mm), strong spatial velocity gradients were present. Velocity gradients became considerably smaller at a larger distance from the valve ($x = 160$ mm), where flow developed into a plug-like shape. Flow at the entrance ($x = 212$ mm) of a convergent section of 10 mm length with a linear change in tube diameter from 40 to 15 mm at the outlet was assumed to be spatially accelerated.

For MR velocity mapping, a gradient-echo sequence (FFE) with bipolar velocity encoding gradients was used. The thickness of the slice was 10 mm, and the in-plane pixel resolution was 1.17×1.17 mm² (matrix 256×256 , field of view 300 mm). The flip angle was 20° , the encoding velocity was set to 100 cm/sec, and TE was 5.4 msec. To generate an image sequence mimicking a moving vessel, the original pair of magnitude and phase images was copied nine times, and the center of the image frame was shifted randomly for each copy. Automatic segmentation of each of the three phantom data sets was conducted five times by the same observer on separate occasions.

In Vivo Measurements

Ten healthy volunteers (mean age 36.7 years; range 27–62 years; all male) were investigated as approved by individual informed consent using a Philips Gyroscan ACS-NT 1.5 T (Philips Medical Systems, Best, The Netherlands) whole-body scanner. A circular surface coil was applied to map the axial blood velocities of the ascending aorta at the approximate level of the sinotubular junction. Depending on the heart rate, 22–30 frames were recorded every 30 msec throughout the cardiac cycle using an electrocardiographic (ECG) triggered gradient-echo sequence (FFE) with bipolar velocity-

encoding gradients. The slice selecting direction was chosen for velocity encoding. To avoid phase wraps the maximum velocity sensitivity was adapted individually and ranged from 120 to 200 cm/sec. The thickness of the slice was 10 mm, and the in-plane pixel resolution was 1.17×1.17 mm² (matrix 256×256 , field of view 300 mm). The flip angle was 20° , and TE ranged from 4.9 to 5.3 msec.

A second set of measurements was obtained in another group of 10 volunteers (mean age 27.1 years; range 21–35 years; 3 female) during a single breath-hold lasting for 20 heart beats. Velocity mapping was performed using a fast hybrid phase contrast technique (TFEPI) combining segmented k -space acquisition with EPI readouts (17). Scan parameters were as follows: $1.4 \times 1.4 \times 10$ mm³ (matrix 128×128 , field of view 179 mm) spatial resolution, 30 msec temporal resolution, 20–26 heart phases, velocity encoding in slice-selection direction 120–200 cm/sec, flip angle 15° , TE 7.1–7.5 msec.

The in vivo measurements were evaluated manually by three independent observers in a blinded fashion. Automatic segmentation of the in vivo images was carried out by another group of three independent observers. One observer repeated automatic and manual segmentation three times on separate occasions. In addition, each in vivo image set was automatically traced by one observer with the constraint of using the magnitude frames only.

Statistics

The correlation between flow values calculated from manual and automatic segmentation of the FFE and of the TFEPI measurements was evaluated using the mean difference method described by Bland and Altman (18) and linear regression statistics. Inter-user and intra-user variability was calculated as the within-subjects coefficient of variation.

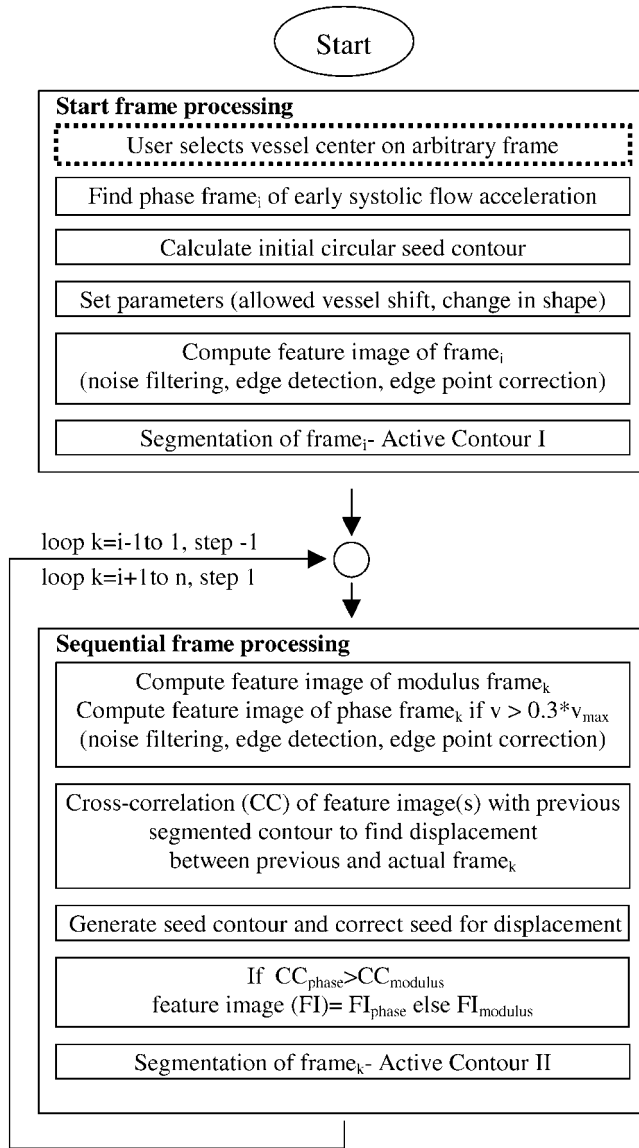


Figure 7. Overview of processing steps for automatic vessel segmentation. The total number of heart phases is denoted by n , v is blood velocity, and v_{\max} is peak blood velocity over all heart phases.

RESULTS

The area calculated from the automatically segmented contours of the three different imaging positions was compared with the area of the Plexiglas tube as shown in Table 1. For the imaging position at 8 mm downstream from the valve, the area was slightly overestimated by 0.7% on average. Area at the second imaging position ($x = 160$ mm) was assessed with an average error of 0.3%. Evaluation of images obtained at the beginning of the convergent geometry resulted in underestimation of luminal area by 0.8%. Phase images were automatically chosen for segmentation for all three imaging positions.

The mean difference of the in vivo flow values calculated from automatically and manually segmented FFE images was -0.9% , and the $\pm 95\%$ limits of agreement were $+3.3\%/-3.2\%$ (Fig. 8). Linear regression resulted

Table 1
Phantom Results*

Position (mm)	Area (mm ²)	Mean error (%)	Variability (%)	
			Intra-series (n = 10)	Intra-observer (n = 5)
$x = 8$	1278.4 ± 1.5	0.72	0.084	0.011
$x = 160$	1271.9 ± 1.6	0.30	0.063	0.037
$x = 212$	1261.4 ± 2.0	0.80	0.064	0.022
"True" area	1269.2			

*Specified area of phantom tube = "true" area. For each distance from the artificial aortic valve ($x = 8, 160, 212$ mm) the acquired image pair was duplicated nine times with a random shift of the image center to mimic a moving vessel. Each image set was automatically segmented five times by the same observer. Area values are mean \pm SD.

in the linear equation $y = 0.97x + 0.17$, and the correlation coefficient r^2 was 0.99. The mean difference of the flow values from automatically vs. manually segmented TFEPI images was -0.9% , and the $\pm 95\%$ limits were $+6.0\%/-5.6\%$ (Fig. 9). Linear regression analysis revealed $y = 0.94x + 0.37$ and a correlation of $r^2 = 0.97$.

The inter-observer variability was 1.9% for manual analysis and 0.5% for automatic analysis of the flow rate obtained with the conventional gradient-echo sequence (FFE). Intra-observer variability of manually segmented images was 0.9% and 0.2% for automatic segmentation of FFE images. Evaluation of images obtained in a single breath-hold with the TFEPI sequence resulted in an inter-observer variability of 1.7%, when done manually, and 0.5% for automatic segmentation; intra-observer variability was 0.7% for manual analysis and 0.3% for automatic analysis (Table 2). Performing automatic segmentation on the FFE images using the magnitude frames only resulted in a mean difference of the flow

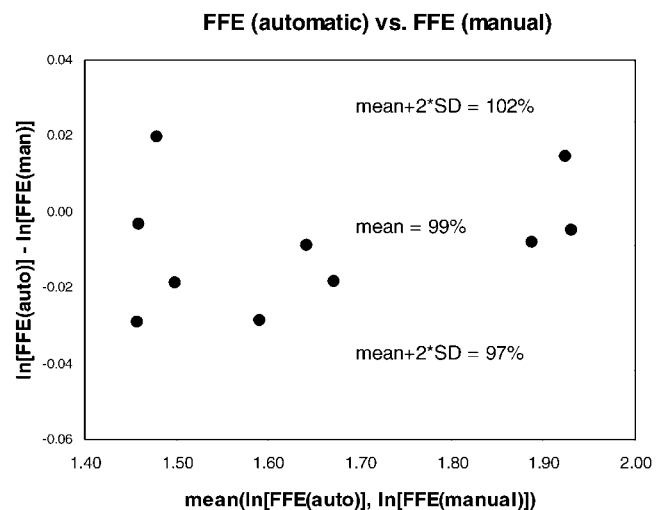


Figure 8. Comparison of volume flow rates obtained from automatically vs. manually traced contours of the images acquired with the conventional gradient-echo (FFE) sequence. The mean value of automatic and manual analysis is plotted along the horizontal axis; the difference between the two methods is plotted along the vertical axis.

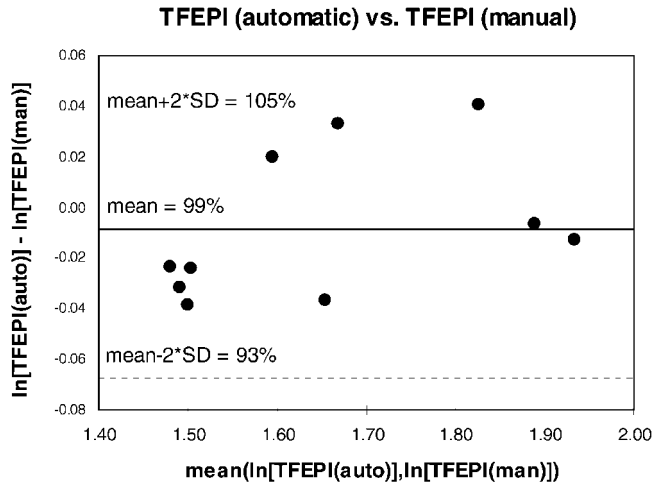


Figure 9. Comparison of volume flow rates obtained from automatically vs. manually traced contours of images acquired with the hybrid phase contrast sequence (TFEPI) within a single breath-hold. The mean value of automatic and manual analysis is plotted along the horizontal axis; the difference between the two methods is plotted along the vertical axis.

values with respect to manual segmentation of -9.29% and $\pm 95\%$ limits of $+20.26\%/-16.56\%$.

DISCUSSION

Using segmentation based on dedicated active contours allows for automatic processing of image frames obtained by phase contrast velocity mapping. Only simple initial user interaction is necessary to start the segmentation.

Initial simulations confirmed the general observation that the phase image is more appropriate for segmentation than the magnitude image under disturbed flow conditions. The phantom validation revealed good agreement in assessing the luminal area for three different flow distributions in a Plexiglas tube. Overestimation of luminal area occurred at the closest position to the valve, where strong spatial velocity variations were present. The flow distribution across the tubular area was characterized by zones of retrograde flow near the hinges of the valve. We therefore attribute parts of the error to the transition from antegrade to retrograde flow.

Table 2
In Vivo Results*

	Variability (%; $n = 3$)	
	Inter-observer	Intra-observer
FFE		
Manual	1.944	0.932
Automatic	0.490	0.175
TFEPI		
Manual	1.718	0.725
Automatic	0.530	0.346

*Three independent users performed manual and automatic segmentation of images obtained in volunteers with a conventional sequence (FFE) and of images acquired with a single breath-hold hybrid technique (TFEPI). Variability is reported as the within-subject coefficient of variation.

Thus, no meaningful edges at these locations could be extracted by the system; accordingly, the contour shape was approximated by the elastic properties of the active contour model. Further downstream, flow was fully antegrade, and the error in assessing luminal area was small. At the beginning of the converging section, flow developed into a plug-like shape. Luminal area calculated from automatically traced contours revealed underestimation. This is probably caused by the effect of spatial acceleration to the signal phase in phase contrast measurements. As described in ref. 19, the time delay between spatial and velocity-encoding gradient gravity centers leads to mapping of velocity within a convergent geometry further downstream with respect to the position of the imaging slice. There are further limitations that apply for the phantom validation. First, signal coming from the surrounding fluid was stationary. This is unlike the in vivo conditions, where moving tissue influences pixel statistics for the threshold determination used in the edge point detection. Second, the edge correction scheme approximates the transition from vessel lumen to wall in a small boundary layer linearly, even though the velocity distribution within the boundary layer is rather parabolic. This probably contributes to the slight overestimation of luminal area seen for two of the three imaging positions. In vivo, about 2500 image frames were processed automatically. Forcing the automatic segmentation to use only the magnitude images led to severe segmentation errors on some of the systolic time frames. Due to the high systolic flow, this resulted in underestimation of the mean flow rate compared with manual segmentation (mean difference $\pm 2SD = -9.3 \pm 20.3\%$).

Using both magnitude and phase, only minor segmentation errors were observed. Flow values in the ascending aorta were calculated accurately using automatic segmentation (mean difference $\pm 2SD = -0.9 \pm 3.3\%$ compared with manual segmentation). Also, flow values from automatically traced images obtained within a single breath-hold agreed well with flow values calculated from manually drawn contours (mean difference $\pm 2SD = -0.9 \pm 6.0\%$).

In this study we only considered flow images obtained in the ascending aorta near the aortic valve. Since the total amount of pixels covering the aortic vessel cross section is large, small deviations between manual and automatic segmentation result in minor change of the volume flow rate. However, the flow distribution near the aortic heart valve is subject to strong spatial and temporal variations and was therefore used to prove the stability of the proposed method. Furthermore, the blood pools surrounding the ascending aorta provide signal intensities comparable to signal within the vessel. This excludes vessel masking as the method of choice for this application.

In vivo validation is also hampered by the use of manual segmentation as a reference. Manual segmentation is still the gold standard even though it suffers from user variability. Fitting a sectorized paraboloid through velocity data as proposed in ref. 20 might be applied for certain time frames obtained in the ascending aorta in

the future. The accuracy of the method in application to the carotid arteries has been reported earlier (21).

The use of both magnitude and phase frames for segmentation assumes that spatial and velocity misregistration (22) of accelerated spins and spins moving in an oblique direction with respect to the gradient axis can be neglected. In particular, the pulsatility of aortic flow might lead to considerable misregistration of velocities due to the finite time between spatial and velocity encoding in the slice-selecting direction. Thus, the velocity map might not correspond to the inflow-weighting seen in the magnitude image of the same time frame, resulting in different contours when traced on the phase and magnitude images, respectively.

Future studies using the method presented should address segmentation of smaller vessels mapped by fewer pixels before the quantitative results of the present study can be fully extrapolated to measurements in other parts of the cardiovascular system.

CONCLUSIONS

The use of dedicated algorithms based on modified active contour models allowed for fast automatic and accurate determination of volume blood flow in the ascending aorta of humans. In combination with single breath-hold phase contrast acquisitions, instantaneous blood flow, volume flow, and dynamic vessel area can be obtained in a fast and reproducible way. The method has potential for the assessment of flow rates in the cardiovascular system.

APPENDIX

Assuming the parameters w_1 and w_2 to be constants and using derivative approximations, the discrete energy functional derived from Eqs. [1] and [2] is written as

$$E = E_{\text{int}}(U) + E_{\text{ext}}(U) = \sum_{i=0}^{N-1} \left\{ \frac{w_1}{2h^2} \|U_{i+1} - U_i\|^2 + \frac{w_2}{2h^4} \|U_{i+1} - 2U_i + U_{i-1}\|^2 + \text{img}(x_i, y_i) \right\}$$

where $U = (x_0 \dots x_{N-1}, y_0 \dots y_{N-1})^T$ represents the contour uniformly sampled at N locations $U_i = (x_i, y_i)^T$, h is the distance between consecutive contour nodes, and $\text{img}()$ is the feature image. Finding U , which is a local minimum for E , is achieved by solving the associated Euler-Lagrange equation (see ref. 13 for a more complete description):

$$U_{i-2} \left(\frac{w_2}{h^4} \right) + U_{i-1} \left(-\frac{4w_2}{h^4} - \frac{w_1}{h^2} \right) + U_i \left(\frac{6w_2}{h^4} + \frac{2w_1}{h^2} \right) + U_{i+1} \left(-\frac{4w_2}{h^4} - \frac{w_1}{h^2} \right) + U_{i+2} \left(\frac{w_2}{h^4} \right) = -\nabla \text{img}(x_i, y_i) = -\left(\frac{\partial}{\partial x_i} \text{img}(x_i, y_i), \frac{\partial}{\partial y_i} \text{img}(x_i, y_i) \right)^T.$$

Since closed contours are considered, we define $U_0 = U_N$, $U_{-1} = U_{N-1}$, etc. and $0 \leq i \leq N-1$. Making the model

dynamic and using matrix notations, the equation given above is written as follows:

$$M\ddot{U} + C\dot{U} + KU = F(U)$$

with

$$F(U) = -\nabla \text{img}(X, Y) =$$

$$-\left(\frac{\partial}{\partial x_0} \text{img}(x_0, y_0), \dots, \frac{\partial}{\partial y_{N-1}} \text{img}(x_{N-1}, y_{N-1}) \right)^T;$$

$$K = \begin{pmatrix} \bar{K} & 0 \\ 0 & \bar{K} \end{pmatrix}; \bar{K} = \begin{pmatrix} a & b & c & \dots \\ b & a & b & \\ c & b & a & \\ \vdots & & & \ddots \end{pmatrix};$$

$$a = \frac{6w_2}{h^4} + \frac{2w_1}{h^2}; b = -\frac{4w_2}{h^4} - \frac{w_1}{h^2}; c = \frac{w_2}{h^4}.$$

$M = \mu I$ assigns the mass density μ to the contour and $C = \lambda I$, where λ is the damping constant, allows the kinetic energy to be dissipated by friction. I denotes the identity matrix. The temporal derivatives of U and the spatial derivatives in $F(U)$ are approximated by finite forward and finite central differences, respectively. With $\mu = 0$ and $F(U_{t+\Delta t}) \cong F(U_t)$, the motion equation of the active contour is obtained as follows:

$$C \frac{U_{t+\Delta t} - U_t}{\Delta t} + KU_{t+\Delta t} \cong F(U_t)$$

$$= -\frac{1}{2} \begin{pmatrix} \text{img}(x_0 + 1, y_0) - \text{img}(x_0 - 1, y_0) \\ \vdots \\ \text{img}(x_{N-1} + 1, y_{N-1}) - \text{img}(x_{N-1} - 1, y_{N-1}) \\ \text{img}(x_0, y_0 + 1) - \text{img}(x_0, y_0 - 1) \\ \vdots \\ \text{img}(x_{N-1}, y_{N-1} + 1) - \text{img}(x_{N-1}, y_{N-1} - 1) \end{pmatrix}$$

REFERENCES

1. Moran PR. A flow velocity zeugmatographic interlace for NMR imaging in humans. *Magn Reson Imaging* 1982;1:197-203.
2. Maier SE, Meier D, Boesiger P, Moser UT, Vieli A. Human abdominal aorta: comparative measurements of blood flow with MR imaging and multigated Doppler US. *Radiology* 1989;171:487-492.
3. Underwood SR, Firmin DN, Rees RS, Longmore DB. Magnetic resonance velocity mapping. *Clin Phys Physiol Meas* 1990;11(suppl A):37-43.
4. Burkart DJ, Felmlee JP, Johnson CD, et al. Cine phase-contrast MR flow measurements: improved precision using an automated method of vessel detection. *J Comput Assist Tomogr* 1994;18:469-475.
5. Kass M, Witkin A, Terzopoulos D. Snakes: active contour models. *J Comput Vision* 1987;1:321-331.
6. Hu YL, Rogers WJ, Coast DA, Kramer CM, Reichel N. Vessel boundary extraction based on variable stiffness deformable model. In: *Proceedings of the 5th Annual Scientific Meeting of the Society of Magnetic Resonance*, Vancouver, 1997. p 52.
7. Lee KY, Yuan C, Hwang JN. Closed contour edge detection for lumen area extraction from phase contrast MR images. In: *Proceedings of the 5th Annual Scientific Meeting of the Society of Magnetic Resonance*, Vancouver, 1997. p 51.

8. Chwialkowski MP, Ibrahim YM, Li HF, Peshock RM. A method for fully automated quantitative analysis of arterial flow using flow-sensitized MR images. *Comput Med Imaging Graph* 1996;20:365–378.
9. Link KM, Lesko NM. The role of MR imaging in the evaluation of acquired diseases of the thoracic aorta. *AJR Am J Roentgenol* 1992;158:1115–1125.
10. Nakayama M, Kyomasu Y, Suzuki Y, et al. Cine MRI of the ascending aorta in the elderly with respect to the flow signal void and aortic valve morphology. *Nippon Ronen Igakkai Zasshi* 1990;27:743–748.
11. Stein PD, Walburn FJ, Sabbah HN. Turbulent stresses in the region of aortic and pulmonary valves. *Trans ASME J Biomech Eng* 1982;104:238–244.
12. Canny J. A computational approach to edge detection. *IEEE Trans Pattern Analysis Machine Intelligence* 1986;8:679–698.
13. Cohen LD. On active contour models and balloons. *CVGIP: Image Understanding* 1991;53:211–218.
14. Perona P, Malik J. Scale-space and edge detection using anisotropic diffusion. *IEEE Trans Pattern Analysis Machine Intelligence* 1990;12:629–639.
15. Ranganath S. Contour extraction from cardiac MRI studies using snakes. *IEEE Trans Med Imaging* 1995;14:328–338.
16. Cohen LD, Cohen I. Finite-element methods for active contour models and balloons for 2-D and 3-D images. *IEEE Trans Pattern Analysis Machine Intelligence* 1993;15:1131–1147.
17. Fischer SE, Wickline SA, Lorenz CH. Multiple slice hybrid imaging sequence for myocardial perfusion measurement. In: *Proceedings of the 4th Annual Scientific Meeting of the Society of Magnetic Resonance*, New York, 1996. p 682.
18. Bland JM, Altman DG. Statistical methods for assessing agreement between two methods of clinical measurement. *Lancet* 1986;1:307–310.
19. Kouwenhoven M, Hofman MB, Sprenger M. Motion induced phase shifts in MR: acceleration effects in quantitative flow measurements—a reconsideration. *Magn Reson Med* 1995;33:766–777.
20. Oyre S, Pedersen EM, Ringgaard S, Boesiger P, Paaske WP. In vivo wall shear stress measured by magnetic resonance velocity mapping in the normal human abdominal aorta. *Eur J Vasc Endovasc Surg* 1997;13:263–271.
21. Oyre S, Ringgaard S, Kozerke S, et al. Quantitation of circumferential subpixel vessel wall position and wall shear stress by multiple sectorized three dimensional paraboloid modeling of velocity encoded cine MRI. *Magn Reson Med* 1998; 40: 645–55.
22. Steinman DA, Ethier CR, Rutt BK. Combined analysis of spatial and velocity displacement artifacts in phase contrast measurements of complex flows. *J Magn Reson Imaging* 1997;7:339–346.